

Cite this: *Environ. Sci.: Nano*, 2024,
11, 4621

Unleashing the power of cobalt pyroborate: superior performance in sulfate radical advanced oxidation processes†

En-Xuan Lin, Fang-Yu Wu, Yu-Lun Zhu, Yu-Rong Chang,
Po-Yi Wu and Pei Yui Keng *

This study presents structurally robust cobalt pyroborate ($\text{Co}_2\text{B}_2\text{O}_5$) as a heterogeneous catalyst for advanced oxidation processes (AOPs). The $\text{Co}_2\text{B}_2\text{O}_5$ nanoparticles were systematically characterized and employed to activate peroxymonosulfate (PMS) effectively in the degradation of various organic recalcitrant pollutants. When compared to conventional heterogeneous CoO and Co_3O_4 catalysts in sulfate radical-advanced oxidation processes (SR-AOPs), the $\text{Co}_2\text{B}_2\text{O}_5$ catalyst exhibited seven-fold and 2.7-fold increases in degradation rate, respectively. The $\text{Co}_2\text{B}_2\text{O}_5$ /PMS system was optimized to enable degradation of a diverse array of persistent organic pollutants, including tetracycline, 4-nitrophenol and sulfamethoxazole, with respective first-order rate constants of 0.136 min^{-1} and 0.104 min^{-1} , and 0.092 min^{-1} , respectively. Mechanistic insights, supported by selective trapping experiments and electron paramagnetic resonance (EPR) analyses, revealed that surface-bound sulfate radicals serve as the primary reactive oxygen species (ROS) under dark conditions. Singlet oxygen species also contributed to the degradation process via a non-radical pathway. Remarkably, the catalyst maintained its effectiveness in the presence of natural organic matter, highlighting its potential practical applicability for wastewater treatment. This study presents the single-component cobalt pyroborate catalyst with high catalytic activity under varying conditions, thus providing unprecedented benefits for industrial wastewater treatment applications.

Received 7th June 2024,
Accepted 28th August 2024

DOI: 10.1039/d4en00516c

rsc.li/es-nano

Environmental significance

The persistence of organic pollutants in wastewater is a critical environmental problem due to their adverse effects on ecosystems and human health. Our study introduces cobalt pyroborate ($\text{Co}_2\text{B}_2\text{O}_5$) nanoparticles as an efficient catalyst for advanced oxidation processes (AOP). This catalyst activates peroxymonosulfate (PMS) to degrade a wide range of recalcitrant organic pollutants, achieving significantly higher degradation rates compared to conventional catalysts. The findings reveal that $\text{Co}_2\text{B}_2\text{O}_5$ effectively degrades pollutants even in the presence of natural organic matter, making it a robust solution for diverse environmental conditions. The environmental significance of this work lies in its potential to enhance water treatment technologies, thereby safeguarding environmental and human health through improved pollutant removal.

1. Introduction

The escalating growth of the global population and industrial activities has led to increased consumption and release of hazardous organic contaminants, including pharmaceuticals, antibiotics, endocrine disruptors, dyes, and pesticides. These pollutants pose significant threat to both human health and ecological stability.^{1,2} Traditional wastewater treatment methods

such as coagulation, precipitation, electrolysis, sedimentation, ion exchange, adsorption, and chlorination³ often fail to effectively degrade recalcitrant toxic organic pollutants such as pharmaceuticals, pesticides, dyes, and phenols.⁴

Advanced oxidation processes (AOPs) and photocatalytic technologies have emerged as powerful methods for degrading toxic organic compounds in wastewater.^{5,6} In particular, AOPs generate highly reactive radicals that can convert hazardous organic compounds into non-toxic metabolites.⁷ Among AOPs, sulfate radical-based advanced oxidation processes (SR-AOPs) have gained attention due to their ability to generate a broad spectrum of reactive oxygen species, including sulfate radicals, which have higher oxidation potential than hydroxyl radicals.⁸ These radicals effectively degrade persistent organic pollutants

Department of Materials Science and Engineering, National Tsing Hua University, Hsinchu 30013, Taiwan. E-mail: keng.py@gapp.nthu.edu.tw; Fax: +886 3 5722366; Tel: +886 3 5715131 ext. 33884

† Electronic supplementary information (ESI) available. See DOI: <https://doi.org/10.1039/d4en00516c>

and have longer half-lives, providing an extended reactive window.^{9,10} Furthermore, SR-AOPs offer greater selectivity in contaminant degradation, reducing the formation of undesirable by-products.¹¹ Consequently, enhancing SR-AOP technologies is a key focus in contemporary wastewater treatment research.

Various activation techniques have been employed to generate sulfate radicals within SR-AOPs, including both physical and chemical methods. These methods activate and cleave the peroxide bonds of oxidants like persulfate (PS) and peroxymonosulfate (PMS). Among chemical activators, transition metals such as Ti, Co, Fe, and Zn have shown remarkable efficacy as catalysts.^{12,13} Specifically, the Co²⁺/PMS system^{14,15} is a benchmark catalyst due to its superior standard electrode potential (Co³⁺/Co²⁺: 1.82 V) compared to iron (Fe³⁺/Fe²⁺: 0.77 V) and copper (Cu²⁺/Cu⁺: 0.16 V) systems.¹⁶ To address the toxicity concerns associated with homogeneous Co²⁺ ions, recent research has developed heterogeneous catalysts such as Co₃O₄, though its catalytic activity remains sub-optimal.^{5,17,18} Current investigations focus on synergistic approaches that combine Co₃O₄ with various materials and elements, such as TiO₂,¹⁹ ZnO,²⁰ Co₃O₄@Co₃O₄/Fe₃O₄ yolk-shell nanostructures,²¹ Co₃O₄/BiOBr,²² graphitic carbon nitride,²³ and reduced graphene oxide (rGO),²⁴ to enhance the electron transfer mechanism, accelerate Co redox cycling, and increase the availability of surface-active sites during sulfate SR-AOPs. These heterostructures, surpassing the performance of heterogeneous CoO and Co₃O₄, represent a notable leap in efficacy. However, the application of these Co-based heterostructures in industrial wastewater treatment is hindered by challenges related to stability and synthetic complexity.^{23,25,26} A comprehensive comparison of these innovative approaches with our current research is delineated in Table S1.†

Addressing these complexities, this paper explores the synthesis of cobalt pyroborate (Co₂B₂O₆) as a single-component heterogeneous catalyst for rapid degradation of persistent pollutants. Transition metal borates have previously been employed as an anode in sodium-ion batteries,²⁷ and in electrocatalytic water splitting applications.^{28–32} In the electrocatalytic water splitting reaction, the borate ligand of the transition metal borate electrode has been shown to weaken the metal–metal bonding and simultaneously reduce the thermodynamic and kinetic barrier for the formation of the required OOH intermediates.³³ Moreover, the borate ligands provide efficient charge transfer and conductivity, thus enhancing the electrical performance of oxygen evolution reaction (OER). In the field of AOPs, the Wang group discovered the peculiar activity of amorphous boron in activating PMS generating highly reactive ROS in the degradation of organic pollutants.^{34–36} This work led to a series of studies demonstrating amorphous boron as a cocatalyst in accelerating AOPs.^{37,38} More recently, Zhou *et al.* reported a fast and long-lasting Fenton reaction for an Fe³⁺ system using metal boride as a cocatalyst. Our previous work showed that carbon, nitrogen-doped iron borate significantly outperformed its oxide counterparts as Fenton catalysts in the degradation of

methylene blue, achieving a ten-fold increase in degradation rate.³⁹ Building upon the superior activity of iron borate, and the promising attributes of boron, metal borate and metal boride, this study explores the potential of cobalt borate in activating PMS in sulfate-radical AOPs. We present the synthesis and characterization of crystalline Co₂B₂O₆ as a potent PMS activator, synthesized through a simple calcination method under ambient pressure. This catalyst achieved rapid and effective degradation of persistent pollutants such as tetracycline, 4-nitrophenol, and sulfamethoxazole, with efficiencies exceeding 95% within 30 minutes, surpassing the degradation efficiency of the metal oxide counterpart.

2. Materials and methods

2.1 Materials and instrumentation

Cobalt(II) oxide (99+, 325 mesh, CoO) was purchased from ACROS. 4-Nitrophenol (99%, 4-NP), boric acid (99.99%, H₃BO₃), cobalt acetate tetrahydrate (98%, Co(CH₃COO)₂·4H₂O), dichloromethane (99.7%, DCM), potassium monopersulfate triple salt (PMS, 2KHSO₅·KHSO₄·K₂SO₄ purity), and sodium nitrate (98+, NaNO₃) were purchased from Alfa Aesar and used as received. Sodium carbonate (99%, Na₂CO₃) was obtained from Honeywell. Sodium phosphate dibasic anhydrous (99%, Na₂HPO₄) was acquired from J. T. Baker. 5,5-Dimethyl-1-pyrroline-*N*-oxide (98%, DMPO) was obtained from Matrix Scientific. Silicon wafer (p-type, boron dopant) was obtained from MUSTEC CORP. Cobalt(II,III) oxide nanopowder (<50 nm particle size, 99.5% trace metals basis, Co₃O₄), ethanol (99.8%, EtOH), sodium chloride (99%, NaCl), sulfamethoxazole (SMX), sodium phosphate monobasic monohydrate (98%, NaH₂PO₄·H₂O) and tetracycline hydrochloride (TC) were obtained from Sigma Aldrich and used as received. Sodium sulfate (99+, Na₂SO₄) and *tert*-butyl alcohol (99+, TBA) were purchased from Thermo Fisher. Deionized water with resistivity of 18.2 MΩ cm was used in all experiments.

Degradation experiments were performed in the absence of light by wrapping the beaker using an aluminum foil. The morphology of the Co₂B₂O₅ sample was analyzed using a transmission electron microscope (TEM, Jeol, JEM-ARM200FTH, 200 k eV). The X-ray diffraction (XRD) patterns were obtained using a Bruker D2 spectrometer with Cu Kα radiation (λ = 1.5418 Å) from 10–70° at a scanning speed of 0.2° s⁻¹ at room temperature. The XRD spectrum was analyzed by MDI Jade software. The optical absorption spectra were determined by a UV-vis spectrometer (HITACHI, U-3900). High-resolution X-ray photoelectron spectroscopy (XPS; ULVAC-PHI, PHI Quantera II) was performed using Al Kα irradiation, and the morphology, particle size and chemical composition were analyzed under a field emission scanning electron microscope (FESEM; Hitachi SU-8010) equipped with energy dispersive X-ray (EDS) mapping equipment. For XPS analysis, the binding energy was calibrated to the carbon peak at 284.5 eV. XPS peak deconvolution and fitting were performed using the CASA XPS software with U2 Tougaard background fitting. The bonding characteristics of the Co₂B₂O₅ samples were examined *via* Fourier-transform

infrared (FTIR) spectroscopy (Bruker Vertex 80v). To prepare the FTIR sample, 5 mg of purified $\text{Co}_2\text{B}_2\text{O}_5$ powder was mixed with 200 mg of potassium bromide powder and ground using a mortar and pestle. The solid mixture was then pressed into a pellet using a pellet press (Specac, Altas 15 T). A potassium bromide pellet sample was prepared similarly and used as the background sample. The cobalt and boron compositions were measured using an inductively coupled plasma optical emission spectrometer (ICP-MS; Agilent 725). The sample for ICP analysis was prepared by adding 2.5 mg $\text{Co}_2\text{B}_2\text{O}_5$ into 20 ml DI water and dissolved with nitric acid.

2.2 Synthesis of cobalt pyroborate ($\text{Co}_2\text{B}_2\text{O}_5$)

The $\text{Co}_2\text{B}_2\text{O}_5$ sample was synthesized *via* a thermal annealing process, based on an adapted protocol from the literature.²⁷ Cobalt acetate tetrahydrate (498 mg, 2 mmol) and boric acid (183.6 mg, 3 mmol) were dissolved in distilled water (20 mL). The mixture was stirred and heated to 90 °C until complete evaporation occurred. The residue was transferred into a crucible and further dried in an oven set to 80 °C for one hour. Subsequently, the dried sample was placed in a tube furnace and calcined at 800 °C for 12 hours with a ramp rate of 5 °C min^{-1} . The resulting $\text{Co}_2\text{B}_2\text{O}_5$ was obtained as a purple color powder with an approximate yield of 150 mg. The product was purified through three cycles of washing: sonication in deionized water, ethanol, and dichloromethane for 10 minutes each. The purified $\text{Co}_2\text{B}_2\text{O}_5$ was recovered by centrifugation at 6000 rpm for 10 minutes and redissolved in appropriate solvents for further characterization and analyses.²⁷

2.3 Degradation of organic pollutants *via* catalytic oxidation of PMS

The catalytic degradation of organic pollutants, specifically tetracycline (TC), 4-nitrophenol (4-NP), and sulfamethoxazole (SMX), was investigated using $\text{Co}_2\text{B}_2\text{O}_5$ as a catalyst in a 100

mL beaker at room temperature (25 °C). Solutions of TC, 4-NP, and SMX were prepared at concentrations of 50 ppm, 40 ppm, and 10 ppm, respectively, in 40 mL of deionized water. After 30 minutes of magnetic stirring in the dark to reach equilibrium, PMS (10 mL, 1 mM) was added to the solution. Samples (3 mL) were collected at predetermined intervals, filtered through a PTFE membrane, and analyzed for UV-vis absorbance. Mean values were calculated from triplicate experiments, and concentrations were determined using Beer-Lambert's law. For experiments in the dark, the beaker was wrapped in aluminum foil, and light exposure was omitted.

2.4 Reactive oxygen species analysis

To identify the primary reactive oxygen species (ROS) and the degradation pathways in the $\text{Co}_2\text{B}_2\text{O}_5$ /PMS system, a series of trapping reagents were employed. Both methanol (MeOH) and ethanol (EtOH) are known to quench both $\text{SO}_4^{\cdot-}$ and HO^{\cdot} radicals,²⁴ while isopropanol selectively traps OH^{\cdot} radicals.⁴⁰ Trapping experiments followed the same protocol as the degradation reactions, with the addition of 1 mM of the trapping agent to elucidate the dominant degradation pathway.^{24,40}

3. Results and discussion

3.1 Synthesis and structural characterization of $\text{Co}_2\text{B}_2\text{O}_5$ nanoparticles

Cobalt pyroborate ($\text{Co}_2\text{B}_2\text{O}_5$) was synthesized *via* a thermal annealing method in accordance with the established literature.²⁷ Fig. 1a illustrates the X-ray diffraction (XRD) pattern, which presents distinct diffraction peaks at 2θ : 20.50°, 22.27°, 30.31°, 32.23°, 34.82°, and 35.71° (JCPDS 73-1772). These data, in conjunction with prior studies on cobalt borate crystallography, confirm that $\text{Co}_2\text{B}_2\text{O}_5$ adopts a triclinic crystal structure with a $P1(2)$ space group. The unit cell parameters

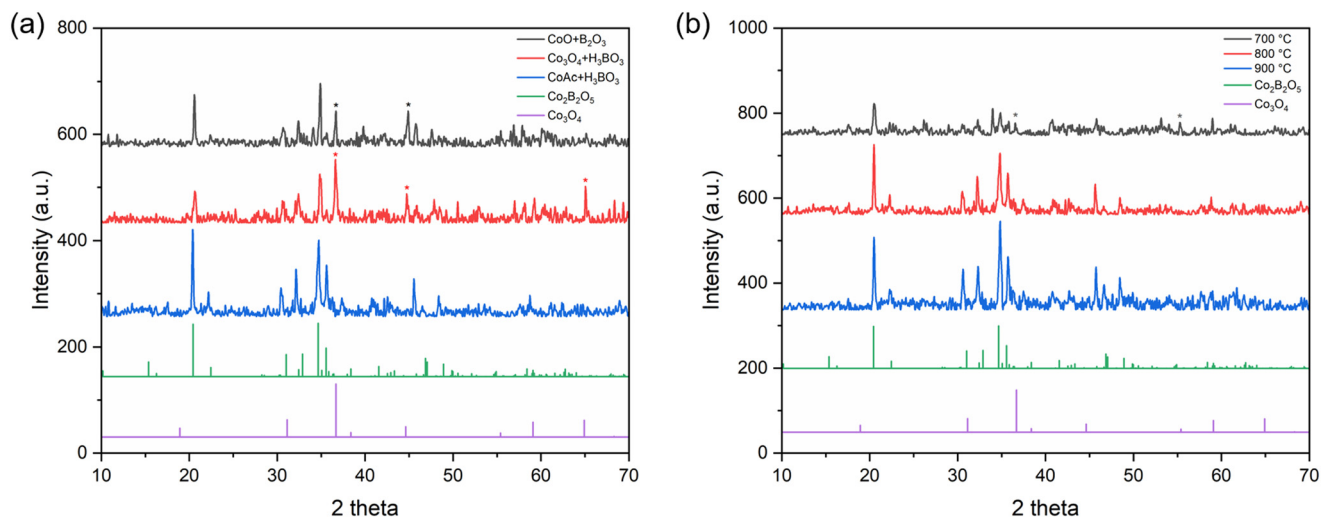


Fig. 1 XRD pattern of (a) $\text{Co}_2\text{B}_2\text{O}_5$ sample synthesized from different precursors and (b) $\text{Co}_2\text{B}_2\text{O}_5$ sample synthesized using cobalt acetate and boric acid at different temperatures.

were reported to be $a = 3.16 \text{ \AA}$, $b = 5.94 \text{ \AA}$, $c = 8.95 \text{ \AA}$, $\alpha = 103.9^\circ$, $\beta = 91.0^\circ$ and $\gamma = 92.0^\circ$.⁴¹

A comparative XRD analysis of samples prepared with various precursors is depicted in Fig. 1a. This analysis reveals that a 2:3 molar ratio of cobalt acetate to boric acid results in the formation of a pure, single-phase crystalline $\text{Co}_2\text{B}_2\text{O}_5$ without any impurities, which matches the XRD pattern of pure $\text{Co}_2\text{B}_2\text{O}_5$ obtained from JCPDS (Fig. 1, green trace). In contrast, using boric acid with either Co_3O_4 or CoO led to residual, unreacted Co_3O_4 , as evidenced by the XRD peaks at $2\theta \sim 36^\circ$, 44° and 65° , which corresponded to the JCPDS XRD pattern for Co_3O_4 (Fig. 1, purple trace). The role of calcination temperature was further explored using cobalt acetate and boric acid as precursors (Fig. 1b). At 700°C , a characteristic, albeit weak, peak for $\text{Co}_2\text{B}_2\text{O}_5$ emerged likely due to inadequate crystallinity. Additionally, impurity peaks corresponding to Co_3O_4 were observed at 2θ values of approximately 36° and 55° , which may arise from the decomposition of $\text{Co}(\text{CH}_3\text{COO})_2 \cdot 4\text{H}_2\text{O}$.⁴² However, an increase in calcination temperature to 800°C resulted in more defined and intensified characteristic peaks for $\text{Co}_2\text{B}_2\text{O}_5$ (Fig. 1b). Fig. S1 in the ESI† offers a detailed structural diagram of $\text{Co}_2\text{B}_2\text{O}_5$, highlighting its tricyclic crystal configuration. In this structure, each Co atom is coordinated to six O atoms, forming a CoO_6 octahedral framework. Within this framework, each Co atom is linked to two BO_3 tetrahedra.^{41,43}

3.2 Morphological and structural characterization of $\text{Co}_2\text{B}_2\text{O}_5$ nanoparticles

High-resolution transmission electron microscopy (HR-TEM), field emission scanning electron microscopy (FESEM), and

energy-dispersive X-ray (EDX) mapping were employed for the morphological and structural analysis of the $\text{Co}_2\text{B}_2\text{O}_5$ sample. The TEM micrograph reveals the $\text{Co}_2\text{B}_2\text{O}_5$ nanoparticles with irregular morphology and an average size distribution of $200 \pm 100 \text{ nm}$. (Fig. 2a). The selected area diffraction (SAED) pattern confirms that the as-prepared $\text{Co}_2\text{B}_2\text{O}_5$ sample possessed a highly crystalline structure (Fig. 2b). The SAED pattern also reveals a lattice spacing of 0.258 nm , which corresponds to the $\{10\text{-}2\}$ plane of $\text{Co}_2\text{B}_2\text{O}_5$ (Fig. 2d).

The Brunauer–Emmett–Teller (BET) analysis of $\text{Co}_2\text{B}_2\text{O}_5$, CoO , and Co_3O_4 , performed using nitrogen (N_2) adsorption at 77 K , revealed distinct differences in their specific surface areas. $\text{Co}_2\text{B}_2\text{O}_5$ exhibited the highest value at $11.2 \text{ m}^2 \text{ g}^{-1}$, followed by CoO at $9.9 \text{ m}^2 \text{ g}^{-1}$, and Co_3O_4 with a significantly lower surface area of $1.12 \text{ m}^2 \text{ g}^{-1}$. The N_2 adsorption–desorption isotherms for the $\text{Co}_2\text{B}_2\text{O}_5$ nanoparticles displayed a type II isotherm with an H3 hysteresis loop, as classified by IUPAC nomenclature.⁴⁴ The type II isotherm is associated with non-porous or macroporous materials, where the initial linear region at low relative pressure indicates monolayer adsorption on the surface, followed by multilayer adsorption as the pressure increases. The presence of an H3 hysteresis loop suggests that the cobalt borate possesses slit-like pores or aggregates of plate-like particles⁴⁴ (Fig. S2†). The presence of plate-like particles is commensurate with the FESEM images of the as-prepared $\text{Co}_2\text{B}_2\text{O}_5$ as shown in Fig. 2e.

The FESEM image illustrates that the $\text{Co}_2\text{B}_2\text{O}_5$ nanoparticles manifest an irregular morphology and sizes (Fig. 2e). EDX analyses further corroborates a homogeneous distribution of Co and O elements throughout the nanoparticle (Fig. 2f and g). Due to the insensitivity of EDX in detecting boron, the following

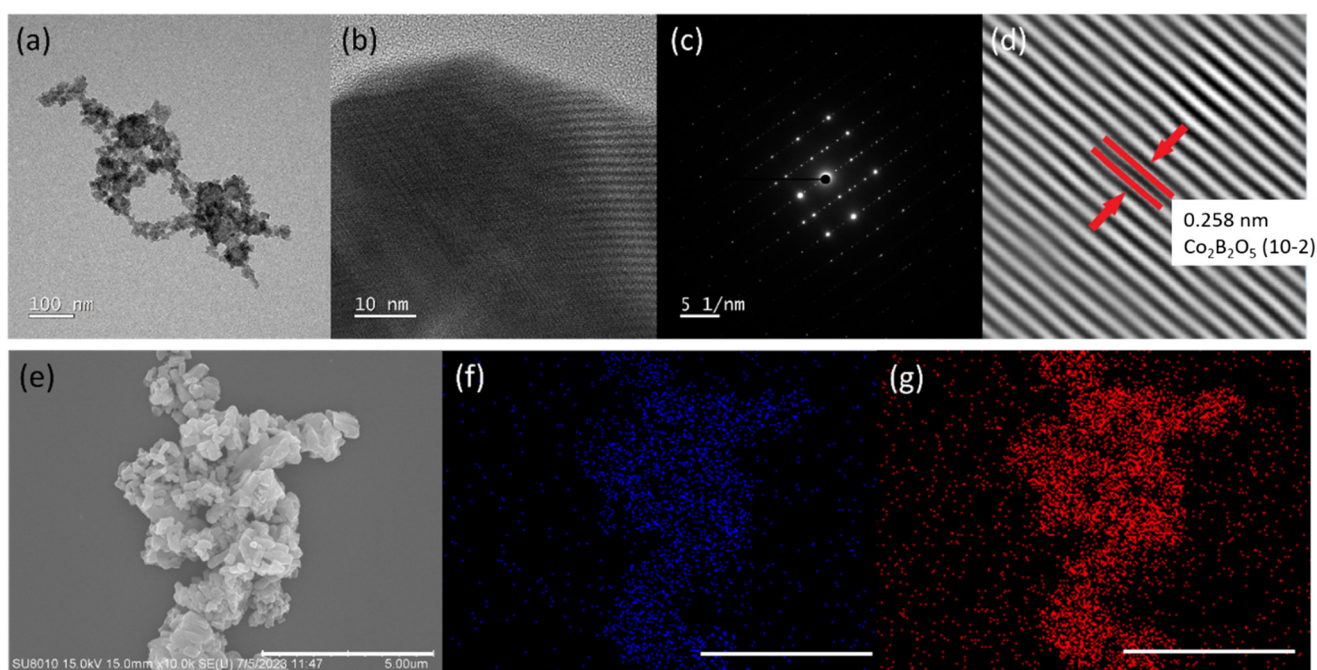


Fig. 2 (a) Low resolution and (b) high resolution TEM images of $\text{Co}_2\text{B}_2\text{O}_5$ particles, (c) diffraction pattern of $\text{Co}_2\text{B}_2\text{O}_5$, (d) d -spacing from HRTEM, (e) FESEM, and EDX mapping of elements (f) Co and (g) O from the FESEM image in (e). Scale bar in (e)–(g) is $5 \mu\text{m}$.

X-ray photoelectron spectroscopy was employed to confirm the synthesis of $\text{Co}_2\text{B}_2\text{O}_5$.

3.3 Spectroscopic analysis

The full survey X-ray photoelectron spectroscopy (XPS) spectrum reveals the presence of Co, B, and O elements in $\text{Co}_2\text{B}_2\text{O}_5$ (Fig. 3a). Gaussian-fitted high-resolution XPS spectra display peaks for Co $2p^{3/2}$ and Co $2p^{1/2}$ at binding energies of 781.4 eV and 797.4 eV, respectively, aligning with literature values for cobalt-based materials (Fig. 3b).⁴⁵ Further deconvolution of Co $2p^{3/2}$ and Co $2p^{1/2}$ revealed two spin orbit doublets, confirming the co-existence of both Co^{2+} and Co^{3+} in the as prepared $\text{Co}_2\text{B}_2\text{O}_5$.^{46,47} The B1s spectrum, centered at 192.0 eV, can be ascribed to B–O bonding, as illustrated in Fig. 3c. Moreover, the O 1s spectrum can be deconvoluted into two distinct components at binding energies of 531.3 eV and 533.1 eV, which correspond to Co–O bonding and B–O bonding, respectively.^{27,45} Fig. S3† shows the Fourier transform infrared (FTIR) spectrum of $\text{Co}_2\text{B}_2\text{O}_5$, revealing several characteristic absorption bands associated with cobalt, boron and oxygen.

3.4 Kinetics of organic pollutant degradation

The degradation efficiency of TC was evaluated in the dark using $\text{Co}_2\text{B}_2\text{O}_5$ as a catalyst for PMS activation, and compared to the efficiencies attained with cobalt oxides as catalysts (Fig. 4). Utilizing the pseudo-first-order kinetic model, $\text{Co}_2\text{B}_2\text{O}_5$

emerged as a superior PMS activator in SR-AOPs, achieving 98% degradation of TC within 25 minutes (Fig. 4). Under identical experiments conditions, Co_3O_4 and CoO achieved only 44% and 77% degradation efficiency, respectively.

3.5 Effect of catalyst and oxidant dosing

In the quest for a versatile and robust catalyst system for the treatment of organic pollutants, it becomes imperative to engineer a system that functions efficiently under varying environmental conditions. Utilizing 4-NP⁴⁸ as a model pollutant, an optimal catalyst dosage of 125 mg L⁻¹ was identified, achieving maximal degradation efficiency with a reaction rate constant of 0.104 min⁻¹ (Fig. 4b). A reduced catalyst concentration of 75 mg L⁻¹ led to a modest decrease in degradation efficacy with a rate constant of 0.062 min⁻¹. Upon establishing the optimal catalyst dosage, the ideal PMS concentration for degrading both 4-NP and SMX⁴⁹ was determined to be 1 mM (Fig. 4c). As shown in Fig. 4c, excessive PMS readily reacted with the highly oxidative $\text{SO}_4^{\cdot-}$, generating the less potent $\text{SO}_5^{\cdot-}$ radicals and thereby limiting further enhancement in degradation efficiency (Fig. 4c).⁵⁰ Based on the optimized $\text{Co}_2\text{B}_2\text{O}_5$ /PMS system, 10 ppm of SMX was completely degraded within 30 minutes (Fig. 4d) with a rate constant of 0.092 min⁻¹. In experiments involving PMS alone (without the addition of $\text{Co}_2\text{B}_2\text{O}_5$ catalyst), a mere 20% degradation of SMX was observed in 30 minutes^{51,52}

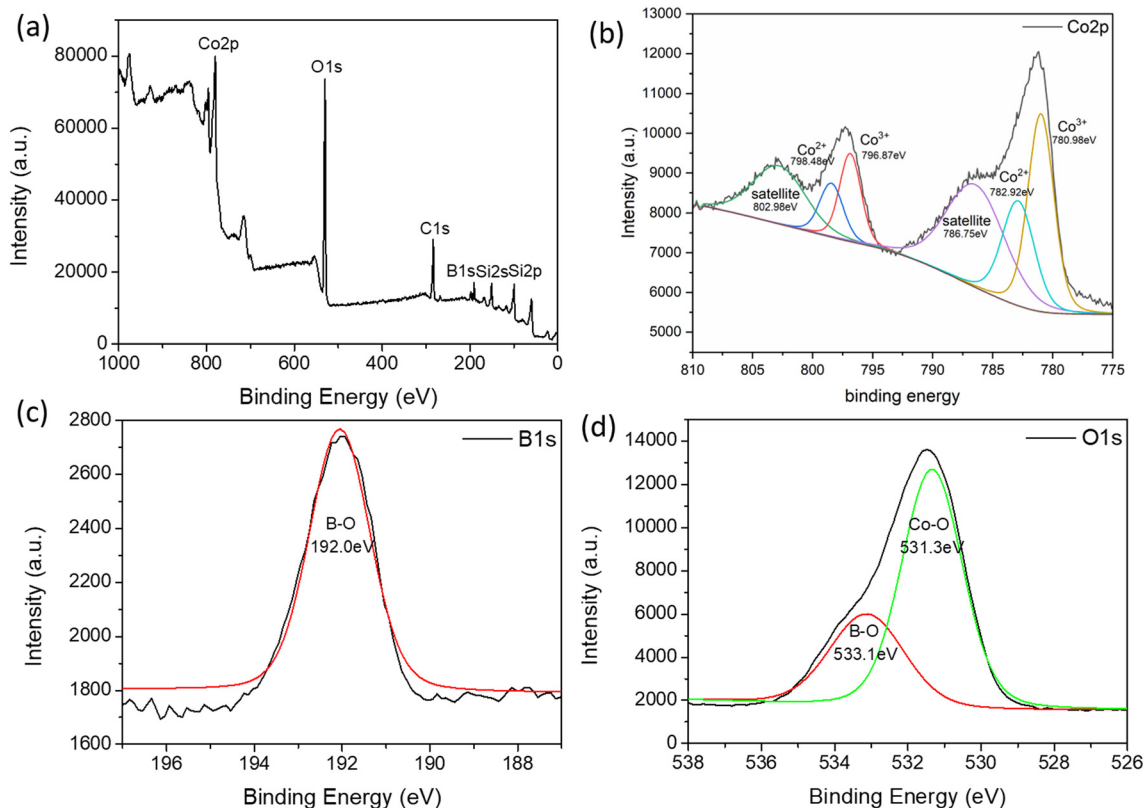


Fig. 3 XPS spectrum of the $\text{Co}_2\text{B}_2\text{O}_5$: (a) full spectrum, (b) Co 2p spectrum, (c) B 1s spectrum and (d) O 1s spectrum.

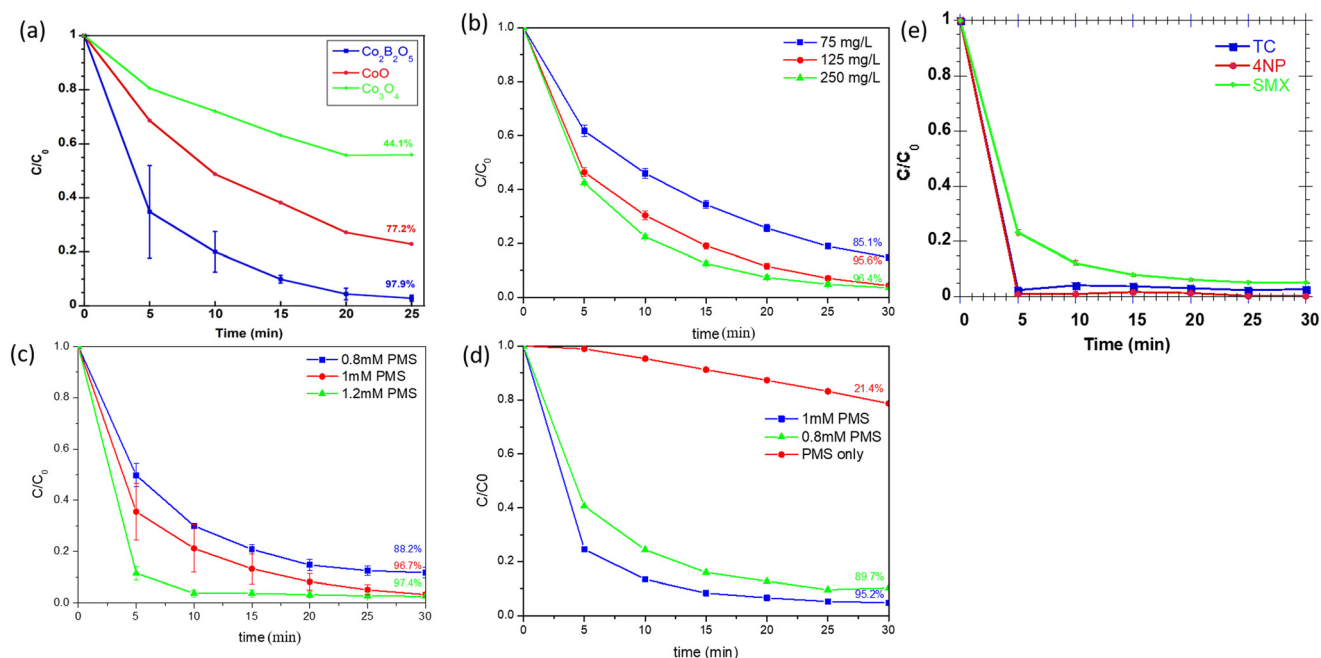


Fig. 4 (a) Kinetic plot for the degradation of TC via SR-AOPs using $\text{Co}_2\text{B}_2\text{O}_5$ (dark blue trace), CoO (red trace) and Co_3O_4 (green trace) as catalysts in the activation of PMS. Reaction conditions: [tetracycline]₀ = 50 ppm; [catalyst] = 125 mg L⁻¹; [PMS] = 1 mM. (b) 4-NP degradation plot using varying amount of catalyst dosage. Reaction conditions: [4-NP]₀ = 40 ppm; [PMS] = 1 mM. (c) 4-NP degradation plot using varying amount of PMS. Reaction conditions: [4-NP]₀ = 50 ppm; [catalyst] = 125 mg L⁻¹. (d) SMX degradation plot using varying amount of PMS. Reaction conditions: [SMX]₀ = 10 ppm; [catalyst] = 125 mg L⁻¹. (e) Comparative degradation rates of TC (blue trace), 4-NP (red trace) and SMX (green trace). Reaction conditions: [pollutant]₀ = 10 ppm; [catalyst] = 125 mg L⁻¹; [PMS] = 1 mM.

with a rate constant of 0.008 min⁻¹. In summary, the $\text{Co}_2\text{B}_2\text{O}_5$ catalyst accelerated the degradation of SMX by a factor of 11.5 compared to PMS alone.

A comparative study was conducted using TC, 4-NP and SMX to access the degradation rates of these organic pollutants in the presence of the $\text{Co}_2\text{B}_2\text{O}_5$ /PMS catalytic system under identical conditions. As illustrated in Fig. 4e, 10 ppm of TC and 4-NP were completely degraded within the

first 5 minutes. Under the same conditions, the degradation of SMX was noticeably slower compared to TC, with a rate constant of 0.092 min⁻¹.

3.6 Surface reaction mechanism of the $\text{Co}_2\text{B}_2\text{O}_5$ /PMS system

To elucidate the surface reaction mechanism of the $\text{Co}_2\text{B}_2\text{O}_5$ /PMS system, this study employs both the Langmuir-Hinshelwood (L-

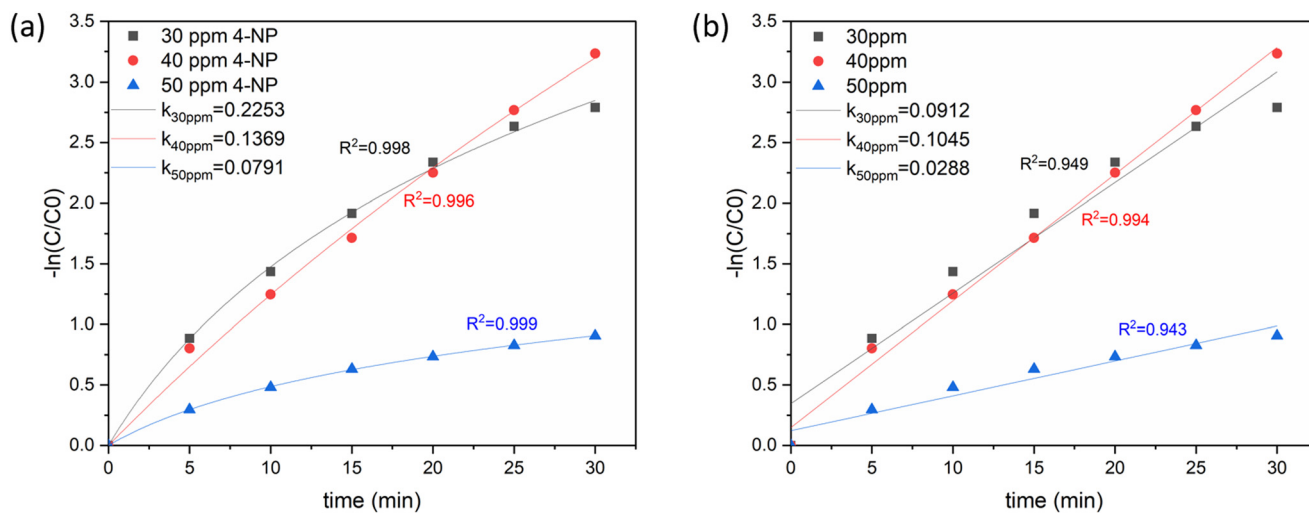


Fig. 5 (a) 4-NP degradation kinetics under different pollutant concentrations; (b) k_s calculation by the L-H model. Reaction conditions: [catalyst] = 125 mg L⁻¹; [PMS] = 1 mM.

H) model and the Eley-Rideal (E-R) model, which are commonly used to describe heterogeneous catalytic reaction mechanisms. The L-H model postulates that both the reactants (PMS) and the pollutant molecules adsorb onto the catalyst's active sites prior to undergoing the reaction.⁵³ Conversely, the E-R model postulates that only the reactant is adsorbed while the pollutant is not, leading to direct reaction with the catalyst.⁵⁴ In this system, the degradation kinetics of the pollutant was found to decrease with increasing pollutant concentration, which is inconsistent with the E-R model (Fig. 5). As a result, the surface reaction rate of $\text{Co}_2\text{B}_2\text{O}_5$ will be evaluated using the L-H model, as described by eqn (1)⁵⁵

$$\frac{1}{k_{\text{obs}}} = \frac{1}{k_s K_{\text{Pollutant}}} + \frac{C_0}{k_s} \quad (1)$$

Here, k_{obs} represents the measured reaction rate derived from degradation experiments, k_s is the initial surface reaction rate, $K_{\text{Pollutant}}$ is the absorption constant for the target pollutant, and C_0 represents the initial pollutant concentration (eqn (1)). To derive k_s and $K_{\text{Pollutant}}$, degradation rates were measured across varying initial concentrations of 4-NP. Fig. 5b illustrates these

results, revealing an initial surface reaction rate (k_s) of $5.747 \text{ mg L}^{-1} \text{ min}^{-1}$, a value considerably higher than those reported for other cobalt-based materials.⁵⁶

3.7 Analysis of the reactive oxygen species

To determine the primary reactive oxygen species (ROS) and the underlying degradation mechanism in the PMS system, trapping experiments were conducted using a variety of selective trapping agents at 1 mM concentration. These trapping experiments were conducted in an identical manner to the degradation of 4-NP, except for the addition of 1 mM of a selective trapping agent. The addition of *tert*-butanol, a common scavenger for aqueous HO^\bullet , exhibited negligible inhibitory effect, suggesting that HO^\bullet is not the main ROS involved in the degradation reaction⁵⁷ (Fig. 6a). Conversely, the addition of methanol, a common scavenger for both aqueous HO^\bullet and $\text{SO}_4^{\bullet-}$, significantly reduces the degradation efficiency of 4-NP from 96.1% to 71.8%, suggesting the crucial role of sulfate radical in this $\text{Co}_2\text{B}_2\text{O}_5/\text{PMS}$ system.⁵⁷

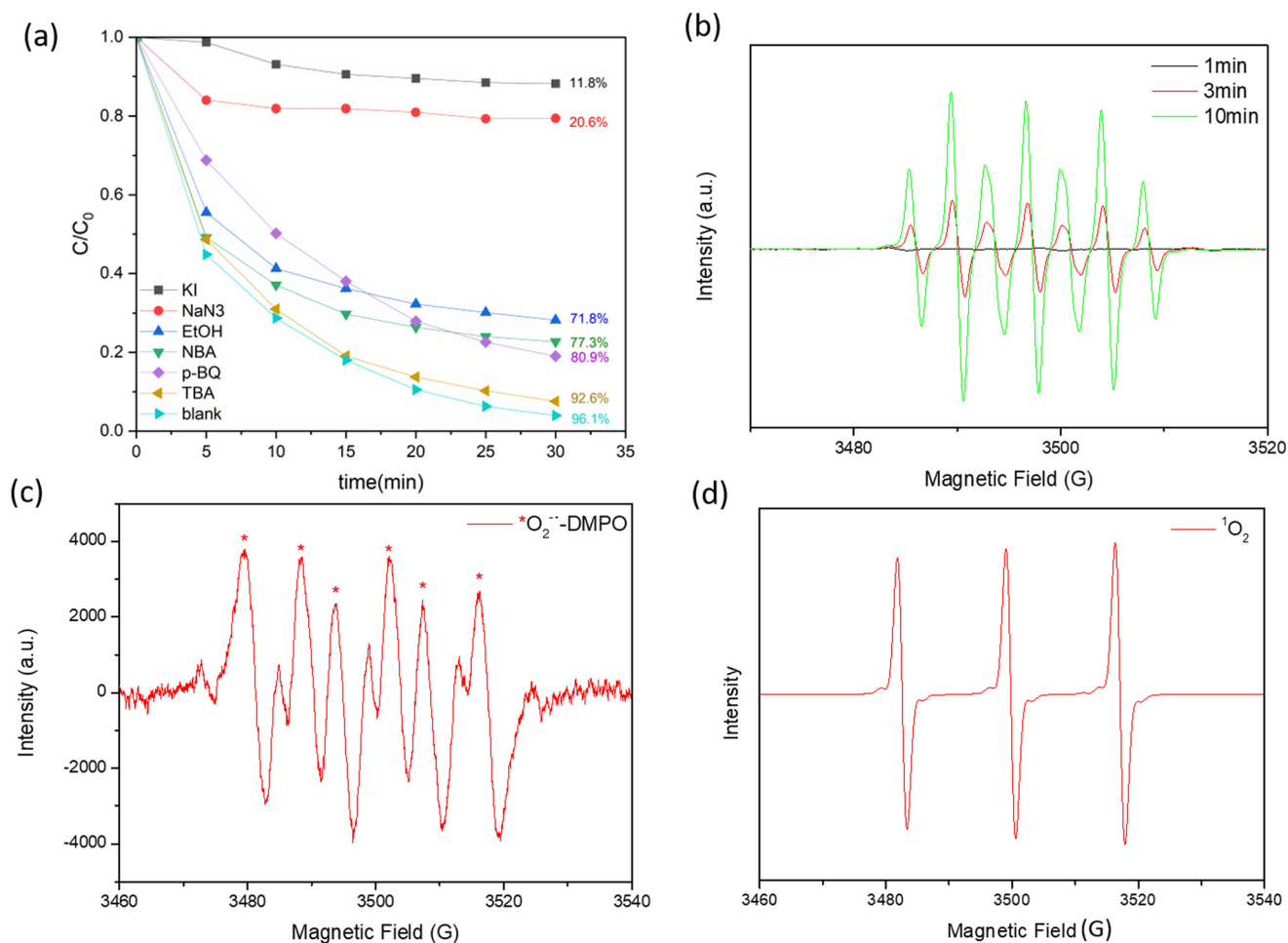


Fig. 6 (a) Kinetic plot of trapping experiments. Reaction conditions: $[4\text{-NP}]_0 = 40 \text{ ppm}$; $[\text{catalyst}] = 125 \text{ mg L}^{-1}$; $[\text{PMS}] = 1 \text{ mM}$; $[\text{trapping agent}] = 1 \text{ mM}$. EPR spectra of (b) DMPOX, (c) DMPO- $\text{O}_2^{\bullet-}$ adduct and (d) TEMP- $^1\text{O}_2$ adduct.

To substantiate that $\text{Co}_2\text{B}_2\text{O}_5$ engages in heterogeneous catalysis, potassium iodide (KI) was introduced to selectively trap the surface-bound $\text{SO}_4^{\cdot-}$ and HO^{\cdot} reactive oxygen species (ROS).⁵⁸ Following the incorporation of KI, a marked decline in the degradation efficiency of 4-NP was observed (Fig. 6a). This data corroborates our hypothesis that the primary degradation agents are the surface-bound radicals $\text{SO}_4^{\cdot-}$ and HO^{\cdot} . Moreover, the inhibitory effect of *n*-butanol (NBA), a trapping agent for surface-bound HO^{\cdot} , was found to be inferior to that of KI. This observation suggests that surface-bound $\text{SO}_4^{\cdot-}$ serves as the dominant ROS in the $\text{Co}_2\text{B}_2\text{O}_5$ /peroxymonosulfate (PMS) system, while other ROS, including surface-bound HO^{\cdot} , aqueous $\text{SO}_4^{\cdot-}$, and aqueous HO^{\cdot} , play subsidiary roles in organic pollutant degradation (Fig. 6a).⁵⁹ Furthermore, we confirmed the role of singlet oxygen ($^1\text{O}_2$) and superoxide ($\text{O}_2^{\cdot-}$) in the $\text{Co}_2\text{B}_2\text{O}_5$ /PMS system by inhibiting the degradation using NaN_3 and *p*-benzoquinone (*p*-BQ), respectively. According to the literature, $^1\text{O}_2$ can be produced through a series of reactions starting from the reaction between HSO_5^- and OH^{\cdot} forming HO_2^{\cdot} . Subsequently, HO_2^{\cdot} undergoes a dehydrogenation reaction to produce the superoxide radicals, $\text{O}_2^{\cdot-}$.^{7,60} Based on these trapping experiments, the inhibitory effect for the $\text{Co}_2\text{B}_2\text{O}_5$ /PMS system was found to be as follows: $^1\text{O}_2 > \text{surface-bound } \text{SO}_4^{\cdot-} > \text{surface-bound } \text{HO}^{\cdot} > \text{free } \text{SO}_4^{\cdot-} > \text{O}_2^{\cdot-} > \text{free } \text{HO}^{\cdot}$. Our results align with the SR-AOPs of Co-based catalysts, in which the non-radical pathway plays the most dominant role. Interestingly, the order of ROS participating in the CoO/PMS system differs from $\text{Co}_2\text{B}_2\text{O}_5$. In the CoO/PMS system, the main ROS is dominated by $^1\text{O}_2$, followed by the surface-bound HO^{\cdot} , while the surface-bound $\text{SO}_4^{\cdot-}$ plays a minor role (Fig. S3†). This distinction highlights the unique catalytic behavior of $\text{Co}_2\text{B}_2\text{O}_5$ in catalyzing SR-AOPs compared to the conventional CoO system. The predominance of surface-bound $\text{SO}_4^{\cdot-}$ radicals in the $\text{Co}_2\text{B}_2\text{O}_5$ /PMS system suggests a more effective pathway for the oxidative degradation of pollutants, given the higher reactivity of $\text{SO}_4^{\cdot-}$ radicals towards electron rich pollutants.⁶¹

To further identify of dominant ROS and establish the role of $^1\text{O}_2$ in the $\text{Co}_2\text{B}_2\text{O}_5$ /PMS AOPs, electron paramagnetic resonance (EPR) experiments were performed using DMPO and TEMP as spin traps (Fig. 6b–d). DMPO was used to detect the production of HO^{\cdot} and $\text{SO}_4^{\cdot-}$ radicals through the formation of DMPO– HO^{\cdot} and DMPO– $\text{SO}_4^{\cdot-}$ adducts, respectively, while TEMP was utilized to trap the $^1\text{O}_2$ species. Contrary to expectation, the EPR results, as presented in Fig. 6b, did not exhibit the characteristic 1:2:2:1 quartet signal of the DMPO– HO^{\cdot} adduct nor the 1:1:1:1:1:1 sextet signal of the DMPO– $\text{SO}_4^{\cdot-}$ adduct. Instead, the EPR spectra, obtained using DMPO as the spin trap, displayed an intense signal indicative of DMPO–X (Fig. 6b). This result may be attributed to the rapid and efficient activation of PMS, which leads to the considerable production of HO^{\cdot} and $\text{SO}_4^{\cdot-}$ radicals, as reported in previous studies.⁶² Moreover, PMS could be quenched through surface oxidation reactions.⁶³ Both of these phenomena contribute to the rapid radical PMS quenching, which explained the absence of DMPO– HO^{\cdot} and DMPO– $\text{SO}_4^{\cdot-}$ adducts in the EPR analyses. Nevertheless, characteristic signals corresponding to DMPOX were observed,

which suggest the coexistence of $\text{SO}_4^{\cdot-}$ and HO^{\cdot} radicals (Fig. 6b).^{51,52} Additionally, the use of DMPO and methanol as spin traps resulted in the appearance of six peaks, indicative of DMPO– $\text{O}_2^{\cdot-}$ adducts, thereby corroborating the presence of $\text{O}_2^{\cdot-}$ (Fig. 6c). Finally, the detection of a TEMP– $^1\text{O}_2$ adduct, evidenced by a characteristic triple peak, confirmed that the $\text{Co}_2\text{B}_2\text{O}_5$ /PMS system also produces $^1\text{O}_2$ ROS through a non-radical pathway (Fig. 6d).

3.8 Effect of the coexistence of natural organic matter (NOM)

The presence of natural organic matter (NOM) and organic pollutants in wastewater can profoundly influence advanced oxidation processes (AOPs) mediated by hydroxyl (HO^{\cdot}) and sulfate radicals ($\text{SO}_4^{\cdot-}$).⁵² To investigate the effect of these naturally occurring anions on the $\text{Co}_2\text{B}_2\text{O}_5$ /PMS treatment system, degradation experiments were carried out in the presence of 10 mM of common anions such as SO_4^- , CO_3^{2-} , Cl^- , and HPO_4^{2-} .^{24,52} The incorporation of Cl^- , CO_3^{2-} and HPO_4^{2-} led to negligible declines in the degradation of 4-NP, with only 1.9%, 3.9% and 8% reduction in pollutant removal efficiency, respectively (Fig. 7a). Compared to the conventional CoO catalyst, the addition of anions, such as CO_3^{2-} , Cl^- , SO_4^{2-} , and HPO_4^{2-} , resulted in notable reduction in the degradation efficiency—by 8.3%, 11.3%, 13.9%, and 28.5%, respectively (Fig. 7b). Our results here suggest that the $\text{Co}_2\text{B}_2\text{O}_5$ /PMS system exhibits robust performance in practical wastewater treatment scenarios, showing minimal sensitivity to halogens or salts.

3.9 Stability of $\text{Co}_2\text{B}_2\text{O}_5$ catalyst

The stability of a catalyst constitutes a critical factor determining its applicability in practical applications. To ascertain the longevity and performance retention of the $\text{Co}_2\text{B}_2\text{O}_5$ catalyst, and its ability to maintain catalytic performance after repeated use, stability tests were conducted (Fig. 8) The catalyst retained 87.5% of its initial efficiency after three catalytic cycles of reuse, demonstrating its stability and reusability.

3.10 Catalytic mechanism of $\text{Co}_2\text{B}_2\text{O}_5$ /PMS AOPs

Upon addition of PMS into the $\text{Co}_2\text{B}_2\text{O}_5$ nanoparticle suspension, the HSO_5^- anion interacts with active sites on $\text{Co}_2\text{B}_2\text{O}_5$ via electron transfer, generating $\text{SO}_4^{\cdot-}$ and HO^{\cdot} radicals on the catalyst's surface (eqn (2)). With a redox potential of 1.84 V for the Co(III)/Co(II) pair, compared to 1.10 V for $\text{HSO}_5^-/\text{SO}_5^{\cdot-}$, redox cycling between Co(III) and HSO_5^- occurs, perpetuating the catalyst's activity (eqn (3)).⁴⁰

To confirm the role of the Co(III)/(II) site in catalyzing the activation of PMS, the XPS of the Co 2p spectrum is compared between the pristine $\text{Co}_2\text{B}_2\text{O}_5$ and the spent catalyst (Fig. 9). In this study, we observed that the relative atomic percentage of Co^{2+} in the spent $\text{Co}_2\text{B}_2\text{O}_5$ increased after the catalytic reactions, while the relative percentage of Co^{3+} decreases (Fig. 9 and Table S3†). Notably, the surface composition of boron disappeared following the degradation reaction, whereas the O 1s XPS spectrum remained

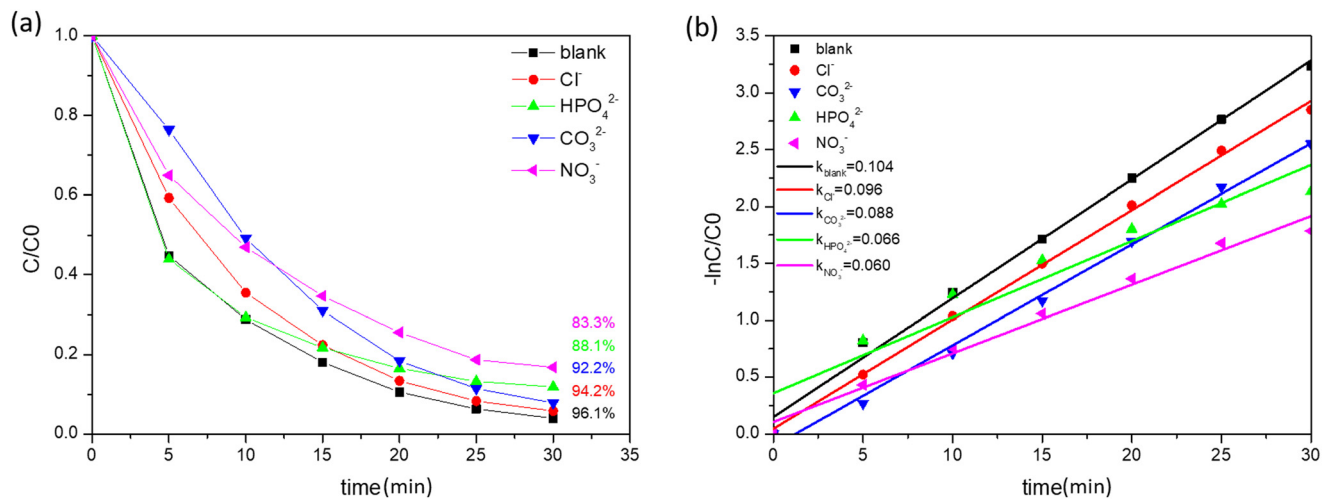


Fig. 7 Comparative evaluation of natural organic matter (NOM) impact on degradation efficiency. Influence of various anions on 4-NP removal using (a) $\text{Co}_2\text{B}_2\text{O}_5$ and (b) CoO under similar experimental conditions involving different anions. Reaction conditions: $[\text{4-NP}]_0 = 50$ ppm; $[\text{catalyst}] = 125$ mg L^{-1} , $[\text{PMS}] = 1$ mM, $[\text{NOM}] = 10$ mM.

unchanged. These findings underscore the critical role of surface borate in the $\text{Co}_2\text{B}_2\text{O}_5$ -catalyzed SR-AOPs, while suggesting a minimal contribution from the oxygen species (Fig. 9). According to research on metal borates as electrocatalysts in water splitting it is suggested that the electron-rich borate ligand functions as an electron donor in catalytic reactions. This electron donation accelerates key electrochemical processes, thereby enhancing the catalyst's overall performance.^{31,64} In the context of SR-AOPs, the presence of a higher relative composition of Co^{2+} of the spent catalyst *versus* the pristine catalyst suggests that the borate ligand served as an electron donor, thereby facilitating the reduction of Co^{3+} to Co^{2+} .^{47,65} Further experimentation is currently underway to fully elucidate the mechanism of electron donation from the borate ligand in $\text{Co}_2\text{B}_2\text{O}_5$ -catalyzed SR-AOPs.

Our experiments further disclose a secondary contribution from HO^\cdot radicals, which likely results from a subsequent reaction between $\text{SO}_4^{\cdot-}$ and H_2O .²⁴ Additionally, $\text{SO}_5^{\cdot-}$, produced from eqn (3), serves as a self-scavenger, continually generating $\text{SO}_4^{\cdot-}$ (eqn (4)).⁶⁶ EPR analyses revealed the production of singlet oxygen ($^1\text{O}_2$) species, which also plays a pivotal role in the $\text{Co}_2\text{B}_2\text{O}_5/\text{PMS}$ system. This non-radical pathway in advanced oxidation processes (AOPs) is highly selective towards unsaturated organic compounds and exhibits extended half-lives in certain solutions, such as phenolic compounds and antibiotics, thereby offering additional degradation pathways.^{67–69} According to the existing literature, $^1\text{O}_2$ may be produced from the reactions starting between HSO_5^- and HO^\cdot , forming HO_2^\cdot (eqn (6)). Subsequently, HO_2^\cdot undergoes a dehydrogenation reaction to yield the superoxide radicals, $\text{O}_2^{\cdot-}$ (ref. 7 and 60) (eqn (7)), which can generate $^1\text{O}_2$ through

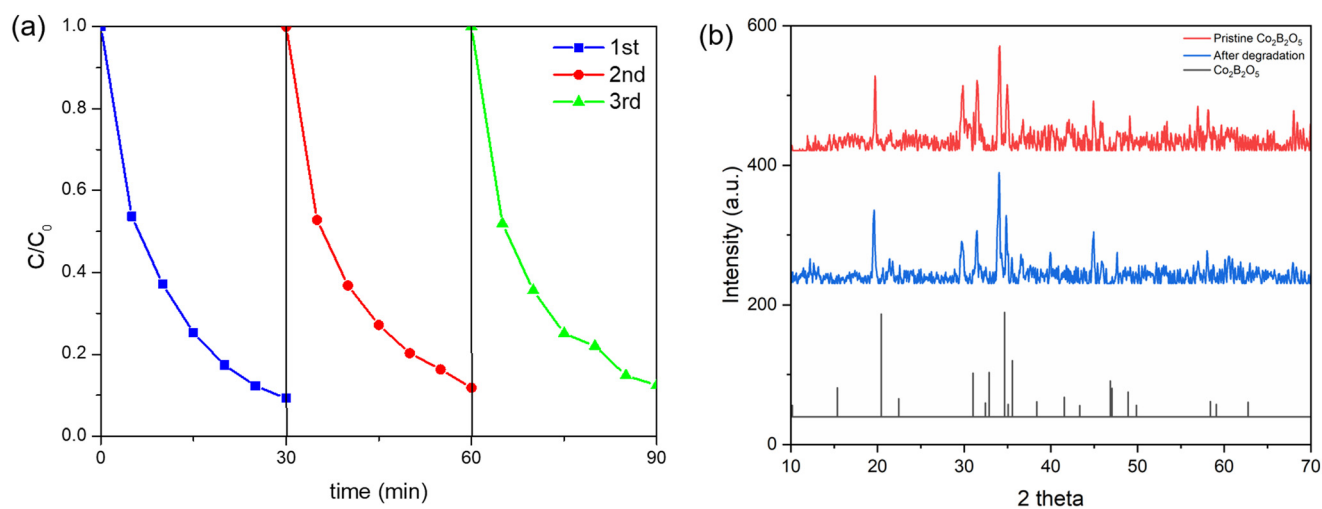


Fig. 8 Stability of the $\text{Co}_2\text{B}_2\text{O}_5/\text{PMS}$ catalyst. (a) 4-NP degradation for three consecutive cycles. (b) XRD of the pristine $\text{Co}_2\text{B}_2\text{O}_5$ catalyst (red trace) and the spent catalyst (blue trace).

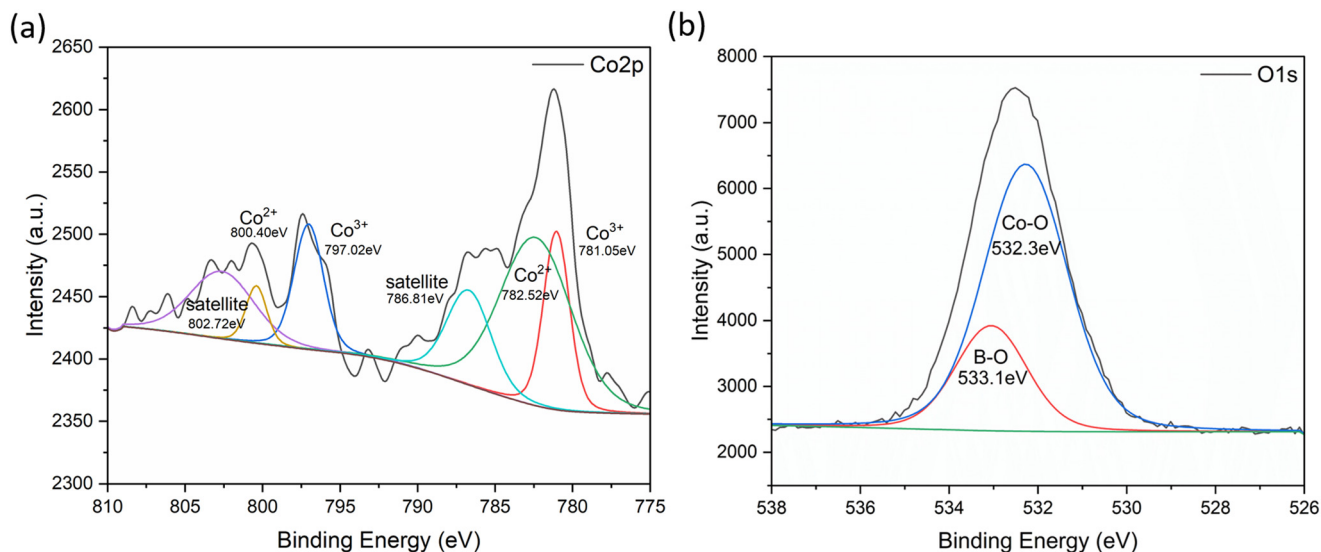
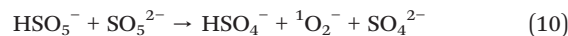
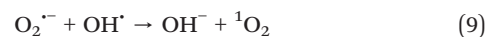
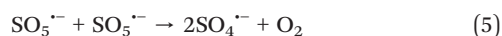
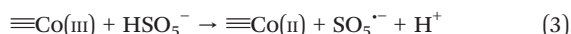
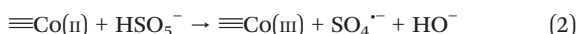


Fig. 9 XPS spectrum of the spent $\text{Co}_2\text{B}_2\text{O}_5$: (a) Co 2p and (b) O 1s spectrum.

multiple processes including self-decomposition and recombination, or reacting with OH^\cdot (ref. 60) (eqn (8)) and (eqn (9)). Lastly, the reaction between HSO_5^- and SO_5^{2-} could also generate a small amount of $^1\text{O}_2$ (ref. 40) (eqn (10)). Based on EPR analyses, trapping experiments, and XPS analyses, we have elucidated a probable degradation pathway for organic pollutants, facilitated by the $\text{Co}_2\text{B}_2\text{O}_5$ catalyst and PMS as shown in Fig. 10.



Conclusions

In this study, we have successfully engineered $\text{Co}_2\text{B}_2\text{O}_5$ as a potent catalyst in activating PMS for the degradation of persistent organic pollutants. Specifically, the $\text{Co}_2\text{B}_2\text{O}_5$ catalyst demonstrated exceptional performance in degrading a range of organic pollutants, including tetracycline, 4-nitrophenol and sulfamethoxazole. Remarkably, the crystalline $\text{Co}_2\text{B}_2\text{O}_5$ catalyst demonstrated 2.6 times and 7 times enhancement in degradation of tetracycline compared to CoO and Co_3O_4 catalysts, respectively, in the oxidation of PMS. The catalyst not only demonstrated structural resilience over multiple cycles but also showed a negligible performance drop in the presence of NOM in wastewater. The increase in catalytic activity is ascribed to the electron-rich borate ligand of the $\text{Co}_2\text{B}_2\text{O}_5$ conduction band, which facilitates the redox cycling of $\text{Co(III)}/\text{Co(II)}$, thereby sustaining the production of reactive oxygen species (ROS). Experimental results confirm that surface-bound sulfate radicals serve as the predominant ROS, in the $\text{Co}_2\text{B}_2\text{O}_5/\text{PMS}$ system, while hydroxy radicals play secondary roles. Consistent with many Co-based catalysts utilized in SR-AOPs, the $\text{Co}_2\text{B}_2\text{O}_5$ catalyst also generates single oxygen species, thereby contributing to the degradation of organic pollutants *via* non-radical pathways. In summary, the present study highlights the promise of $\text{Co}_2\text{B}_2\text{O}_5$ as a potent catalyst for SR-AOPs, which

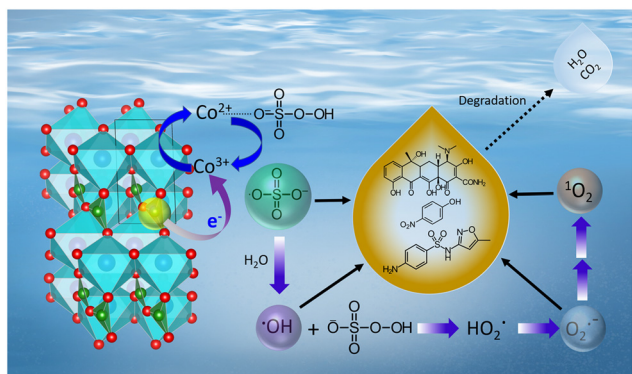


Fig. 10 The overall mechanism of the $\text{Co}_2\text{B}_2\text{O}_5/\text{PMS}$ system for degrading organic pollutants.

simplifies synthetic protocols, eliminating the complexities associated with integrated and composite materials.

Data availability

The data supporting this article have been included as part of the ESI.†

Author contributions

P. Y. K. conceived of the experiments. E. X. L. prepared the samples and conducted the synthesis, characterization and degradation experiment. F. Y. W. optimized the degradation experiment and performed the trapping experiments and the catalyst stability experiment. Y. L. Z. and Y. R. C. conducted the degradation experiments and characterization of the materials. P. Y. W. optimized the degradation experiments and analyses. E. X. L., P. Y. W., F. Y. W. and P. Y. K. analyzed the data and discussed the results. E. X. L. and P. Y. K. wrote the paper.

Conflicts of interest

The authors declare no competing financial interest.

Acknowledgements

The authors would like to acknowledge the National Tsing Hua University (NTHU) Precious Instrumentation Center and the Department of Materials Science Engineering, NTHU in providing HRTEM, XRD, SEM, FTIR, and XPS analyses. The author also acknowledges Prof. Che-Ning Yeh for providing BET surface area analysis. The authors also gratefully acknowledge the financial support provided for this research by the National Science Technology Council, Taiwan, under Grant No. NSTC 111-2124-M-007-003-, NSTC 112-2221-E-007-042.

References

- 1 M. Patel, R. Kumar, K. Kishor, T. Mlsna, C. U. Pittman Jr and D. Mohan, Pharmaceuticals of Emerging Concern in Aquatic Systems: Chemistry, Occurrence, Effects, and Removal Methods, *Chem. Rev.*, 2019, **119**(6), 3510–3673.
- 2 J. A. Rodríguez-Hernández, R. G. Araújo, I. Y. López-Pacheco, L. I. Rodas-Zuluaga, R. B. González-González and L. Parra-Arroyo, *et al.*, Environmental persistence, detection, and mitigation of endocrine disrupting contaminants in wastewater treatment plants – a review with a focus on tertiary treatment technologies, *Environ. Sci.: Adv.*, 2022, **1**(5), 680–704.
- 3 V. K. Gupta, I. Ali, T. A. Saleh, A. Nayak and S. Agarwal, Chemical treatment technologies for waste-water recycling—an overview, *RSC Adv.*, 2012, **2**(16), 6380–6388.
- 4 P. R. Rout, T. C. Zhang, P. Bhunia and R. Y. Surampalli, Treatment technologies for emerging contaminants in wastewater treatment plants: A review, *Sci. Total Environ.*, 2021, **753**, 141990.
- 5 A. Wang, Y. Chen, Z. Zheng, H. Wang, X. Li and Z. Yang, *et al.*, In situ N-doped carbon-coated mulberry-like cobalt manganese oxide boosting for visible light driving photocatalytic degradation of pharmaceutical pollutants, *Chem. Eng. J.*, 2021, **411**, 128497.
- 6 P. Jiang, T. Zhou, J. Bai, Y. Zhang, J. Li and C. Zhou, *et al.*, Nitrogen-containing wastewater fuel cells for total nitrogen removal and energy recovery based on Cl⁻/ClO⁻ oxidation of ammonia nitrogen, *Water Res.*, 2023, **235**, 119914.
- 7 S. Giannakis, K. Y. A. Lin and F. Ghanbari, A review of the recent advances on the treatment of industrial wastewaters by Sulfate Radical-based Advanced Oxidation Processes (SR-AOPs), *Chem. Eng. J.*, 2021, **406**, 127083.
- 8 Q. Yang, H. Choi, S. R. Al-Abed and D. D. Dionysiou, Iron-cobalt mixed oxide nanocatalysts: Heterogeneous peroxymonosulfate activation, cobalt leaching, and ferromagnetic properties for environmental applications, *Appl. Catal., B*, 2009, **88**(3), 462–469.
- 9 Y. Li, S. Zhang, Y. Qin, C. Yao, Q. An and Z. Xiao, *et al.*, Preparation of cobalt/hydrochar using the intrinsic features of rice hulls for dynamic carbamazepine degradation via efficient PMS activation, *J. Environ. Chem. Eng.*, 2022, **10**(6), 108659.
- 10 W. D. Oh, Z. Dong and T. T. Lim, Generation of sulfate radical through heterogeneous catalysis for organic contaminants removal: Current development, challenges and prospects, *Appl. Catal., B*, 2016, **194**, 169–201.
- 11 X. Xia, F. Zhu, J. Li, H. Yang, L. Wei and Q. Li, *et al.*, A Review Study on Sulfate-Radical-Based Advanced Oxidation Processes for Domestic/Industrial Wastewater Treatment: Degradation, Efficiency, and Mechanism, *Front. Chem.*, 2020, **8**, 592056.
- 12 D. Roy, P. Kumar, A. Soni and M. Nemiwal, A versatile and microporous Zn-based MOFs as a recyclable and sustainable heterogeneous catalyst for various organic transformations: A review (2015-present), *Tetrahedron*, 2023, 133408.
- 13 C. Dong, Y. Pang, Y. Chen, Z. Gao, M. Cai and M. Jin, *et al.*, Fe-Ti bimetal catalyst derived from biowaste for highly efficient persulfate activation: Performance and mechanisms, *Process Saf. Environ. Prot.*, 2022, **168**, 654–667.
- 14 J. Wang and S. Wang, Activation of persulfate (PS) and peroxymonosulfate (PMS) and application for the degradation of emerging contaminants, *Chem. Eng. J.*, 2018, **334**, 1502–1517.
- 15 X. Chen, J. Chen, X. Qiao, D. Wang and X. Cai, Performance of nano-Co3O4/peroxymonosulfate system: Kinetics and mechanism study using Acid Orange 7 as a model compound, *Appl. Catal., B*, 2008, **80**(1), 116–121.
- 16 W. D. Oh, V. W. C. Chang, Z. T. Hu, R. Goei and T. T. Lim, Enhancing the catalytic activity of g-C3N4 through Me doping (Me=Cu, Co and Fe) for selective sulfathiazole degradation via redox-based advanced oxidation process, *Chem. Eng. J.*, 2017, **323**, 260–269.
- 17 G. Yi, M. Ye, J. Wu, Y. Wang, Y. Long and G. Fan, Facile chemical blowing synthesis of interconnected N-doped carbon nanosheets coupled with Co3O4 nanoparticles as

- superior peroxymonosulfate activators for p-nitrophenol destruction: Mechanisms and degradation pathways, *Appl. Surf. Sci.*, 2022, **593**, 153244.
- 18 B. Li, Y. F. Wang, L. Zhang and H. Y. Xu, Enhancement strategies for efficient activation of persulfate by heterogeneous cobalt-containing catalysts: A review, *Chemosphere*, 2022, **291**, 132954.
 - 19 X. Jiang, J. Li, J. Li, W. Xu and Z. Liu, Visible-Light-Driven Peroxymonosulfate Activation for Accelerating Tetracycline Removal Using Co-TiO₂ Nanospheres, *Catalysts*, 2023, **13**(5), 836.
 - 20 D. Liu, X. Xue, X. Zhang, Y. Huang and P. Feng, Highly efficient peroxymonosulfate activation by MOFs-derived oxygen vacancy-rich Co₃O₄/ZnO p-n heterojunction nanocomposites to degrade pefloxacin, *Sep. Purif. Technol.*, 2023, **305**, 122451.
 - 21 B. Li, H. Y. Xu, G. H. N. Chi, L. M. Dong, L. W. Shan and L. G. Jin, *et al.*, Integrating the confinement effect and bimetallic cycles in a hierarchical Co₃O₄@Co₃O₄/Fe₃O₄ yolk-shell nanoreactor for peroxymonosulfate activation enhancement, *Chem. Eng. J.*, 2024, **483**, 149403.
 - 22 S. Q. Zhang, H. Y. Xu, B. Li, Y. Xu and S. Komarneni, Constructing a Z-Scheme Co₃O₄/BiOBr Heterojunction to Enhance Photocatalytic Peroxydisulfate Oxidation of High-Concentration Rhodamine B: Mechanism, Degradation Pathways, and Toxicological Evaluations, *Inorg. Chem.*, 2024, **63**(9), 4447–4460.
 - 23 L. Wang, X. Guo, Y. Chen, S. Ai and H. Ding, Cobalt-doped g-C₃N₄ as a heterogeneous catalyst for photo-assisted activation of peroxymonosulfate for the degradation of organic contaminants, *Appl. Surf. Sci.*, 2019, **467–468**, 954–962.
 - 24 L. Amirache, F. Barka-Bouaifel, P. Borthakur, M. R. Das, H. Ahouari and H. Vezin, *et al.*, Cobalt sulfide-reduced graphene oxide: An efficient catalyst for the degradation of rhodamine B and pentachlorophenol using peroxymonosulfate, *J. Environ. Chem. Eng.*, 2021, **9**(5), 106018.
 - 25 E. J. Radich, A. L. Krenselewski, J. Zhu and P. V. Kamat, Is Graphene a Stable Platform for Photocatalysis? Mineralization of Reduced Graphene Oxide With UV-Irradiated TiO₂ Nanoparticles, *Chem. Mater.*, 2014, **26**(15), 4662–4668.
 - 26 B. T. Zhang, Y. Zhang and Y. Teng, Electrospun magnetic cobalt-carbon nanofiber composites with axis-sheath structure for efficient peroxymonosulfate activation, *Appl. Surf. Sci.*, 2018, **452**, 443–450.
 - 27 H. Chen, B. B. Xu, Q. S. Ping, B. Z. Wu, X. K. Wu and Q. Q. Zhuang, *et al.*, Co₂B₂O₅ as an anode material with high capacity for sodium ion batteries, *Rare Met.*, 2020, **39**(9), 1045–1052.
 - 28 Y. Meng, G. Ni, X. Jin, J. Peng and Q. Y. Yan, Recent advances in the application of phosphates and borates as electrocatalysts for water oxidation, *Mater. Today Nano*, 2020, **12**, 100095.
 - 29 T. Tan, P. Han, H. Cong, G. Cheng and W. Luo, An Amorphous Cobalt Borate Nanosheet-Coated Cobalt Boride Hybrid for Highly Efficient Alkaline Water Oxidation Reaction, *ACS Sustainable Chem. Eng.*, 2019, **7**(6), 5620–5625.
 - 30 W. Zhao, T. Xu, T. Li, Y. Wang, H. Liu and J. Feng, *et al.*, Amorphous Iron(III)-Borate Nanolattices as Multifunctional Electrodes for Self-Driven Overall Water Splitting and Rechargeable Zinc-Air Battery, *Small*, 2018, **14**(48), 1802829.
 - 31 L. Cui, W. Zhang, R. Zheng and J. Liu, Electrocatalysts Based on Transition Metal Borides and Borates for the Oxygen Evolution Reaction, *Chem. - Eur. J.*, 2020, **26**(51), 11661–11672.
 - 32 A. M. Ozerova, V. I. Simagina, O. V. Komova, O. V. Netskina, G. V. Odegova and O. A. Bulavchenko, *et al.*, Cobalt borate catalysts for hydrogen production via hydrolysis of sodium borohydride, *J. Alloys Compd.*, 2012, **513**, 266–272.
 - 33 H. Chen, S. Ouyang, M. Zhao, Y. Li and J. Ye, Synergistic Activity of Co and Fe in Amorphous Co_x-Fe-B Catalyst for Efficient Oxygen Evolution Reaction, *ACS Appl. Mater. Interfaces*, 2017, **9**(46), 40333–40343.
 - 34 X. Duan, W. Li, Z. Ao, J. Kang, W. Tian and H. Zhang, *et al.*, Origins of boron catalysis in peroxymonosulfate activation and advanced oxidation, *J. Mater. Chem. A*, 2019, **7**(41), 23904–23913.
 - 35 P. Zhou, Y. Yang, W. Ren, X. Li, Y. Zhang and B. Lai, *et al.*, Molecular and kinetic insights to boron boosted Fenton-like activation of peroxymonosulfate for water decontamination, *Appl. Catal., B*, 2022, **319**, 121916.
 - 36 W. Ren, P. Zhou, G. Nie, C. Cheng, X. Duan and H. Zhang, *et al.*, Hydroxyl radical dominated elimination of plasticizers by peroxymonosulfate on metal-free boron: Kinetics and mechanisms, *Water Res.*, 2020, **186**, 116361.
 - 37 H. Zhou, S. Wu, Y. Zhou, Y. Yang, J. Zhang and L. Luo, *et al.*, Insights into the oxidation of organic contaminants by iron nanoparticles encapsulated within boron and nitrogen co-doped carbon nanoshell: Catalyzed Fenton-like reaction at natural pH, *Environ. Int.*, 2019, **128**, 77–88.
 - 38 A. M. Mesquita, I. R. Guimarães, G. M. M. de Castro, M. A. Gonçalves, T. C. Ramalho and M. C. Guerreiro, Boron as a promoter in the goethite (α -FeOOH) phase: Organic compound degradation by Fenton reaction, *Appl. Catal., B*, 2016, **192**, 286–295.
 - 39 S. Y. Hsiao, E. X. Lin and P. Y. Keng, Facile Synthesis of Carbon- and Nitrogen-Doped Iron Borate as a Highly Efficient Single-Component Heterogeneous Photo-Fenton Catalyst under Simulated Solar Irradiation, *Nanomaterials*, 2021, **11**(11), 2853.
 - 40 Q. Wang, Z. Xu, Y. Cao, Y. Chen, X. Du and Y. Yang, *et al.*, Two-dimensional ultrathin perforated Co₃O₄ nanosheets enhanced PMS-Activated selective oxidation of organic micropollutants in environmental remediation, *Chem. Eng. J.*, 2022, **427**, 131953.
 - 41 S. V. Berger, O. Hassel, M. Webb and M. Rottenberg, The Crystal Structure of Cobaltpyroborate, *Acta Chem. Scand.*, 1950, **4**, 1054–1065.
 - 42 M. A. Mohamed, S. A. Halawy and M. M. Ebrahim, The non-isothermal decomposition of cobalt acetate tetrahydrate, *J. Therm. Anal.*, 1994, **41**(2), 387–404.
 - 43 Combustion synthesis of cobalt pigments: Blue and pink, 2023.

- 44 M. Thommes, K. Kaneko, A. V. Neimark, J. P. Olivier, F. Rodriguez-Reinoso and J. Rouquerol, *et al.*, Physisorption of gases, with special reference to the evaluation of surface area and pore size distribution (IUPAC Technical Report), *Pure Appl. Chem.*, 2015, **87**(9–10), 1051–1069.
- 45 N. A. Kryuchkova, G. A. Kostin, E. V. Korotaev and A. V. Kalinkin, XPS and quantum chemical investigation of electronic structure of Co complexes with calix[4]arenes modified by R2PO groups in upper or lower rim, *J. Electron Spectrosc. Relat. Phenom.*, 2018, **229**, 114–123.
- 46 L. Wu, P. Guo, X. Wang, H. Li, X. Zhang and K. Chen, *et al.*, The synergy of sulfur vacancies and heterostructure on CoS@FeS nanosheets for boosting the peroxymonosulfate activation, *Chem. Eng. J.*, 2022, **446**, 136759.
- 47 H. Xu, D. Wang, J. Ma, T. Zhang, X. Lu and Z. Chen, A superior active and stable spinel sulfide for catalytic peroxymonosulfate oxidation of bisphenol S, *Appl. Catal., B*, 2018, **238**, 557–567.
- 48 W. Pan, G. Zhang, T. Zheng and P. Wang, Degradation of p-nitrophenol using CuO/Al₂O₃ as a Fenton-like catalyst under microwave irradiation, *RSC Adv.*, 2015, **5**(34), 27043–27051.
- 49 X. Zhao, X. Li, Y. Xu, Y. Qi, Q. Wei and X. Jia, Effects of Fe-Co@N-BC anode on degradation of sulfamethoxazole (SMX) in microbial fuel cells, *J. Water Process Eng.*, 2023, **52**, 103569.
- 50 J. Yan, J. Li, J. Peng, H. Zhang, Y. Zhang and B. Lai, Efficient degradation of sulfamethoxazole by the CuO@Al₂O₃ (EPC) coupled PMS system: Optimization, degradation pathways and toxicity evaluation, *Chem. Eng. J.*, 2019, **359**, 1097–1110.
- 51 P. He, C. Gu, B. Tang, Y. Zhou, M. Gan and J. Zhu, Expedient degradation of SMX by high-valent cobalt-oxo species derived from cobalt-doped C₃N₅-activated peroxymonosulfate with the assistance of visible light, *Sep. Purif. Technol.*, 2022, **301**, 122009.
- 52 Y. Li, W. Zhu, Q. Guo, X. Wang, L. Zhang and X. Gao, *et al.*, Highly efficient degradation of sulfamethoxazole (SMX) by activating peroxymonosulfate (PMS) with CoFe₂O₄ in a wide pH range, *Sep. Purif. Technol.*, 2021, **276**, 119403.
- 53 R. K. Narayanan and S. J. Devaki, Brawny Silver-Hydrogel Based Nanocatalyst for Reduction of Nitrophenols: Studies on Kinetics and Mechanism, *Ind. Eng. Chem. Res.*, 2015, **54**(4), 1197–1203.
- 54 X. Ren, L. Tang, J. Wang, E. Almatrafi, H. Feng and X. Tang, *et al.*, Highly efficient catalytic hydrogenation of nitrophenols by sewage sludge derived biochar, *Water Res.*, 2021, **201**, 117360.
- 55 X. Xue, K. Hanna, M. Abdelmoula and N. Deng, Adsorption and oxidation of PCP on the surface of magnetite: Kinetic experiments and spectroscopic investigations, *Appl. Catal., B*, 2009, **89**(3), 432–440.
- 56 G. Bandal, V. Watwe, S. Kulkarni and P. Kulkarni, Effect of addition of surfactant on physicochemical properties of cobalt oxide nanoparticles synthesised using a domestic microwave: Applications as photocatalyst and supercapacitor, *Optik*, 2023, **278**, 170743.
- 57 Y. Tao, Q. Ni, M. Wei, D. Xia, X. Li and A. Xu, Metal-free activation of peroxymonosulfate by g-C₃N₄ under visible light irradiation for the degradation of organic dyes, *RSC Adv.*, 2015, **5**(55), 44128–44136.
- 58 L. Wang, J. Li, X. Liu, J. Zhang, X. Wen and Y. Song, *et al.*, High yield M-BTC type MOFs as precursors to prepare N-doped carbon as peroxymonosulfate activator for removing sulfamethazine: The formation mechanism of surface-bound SO₄^{•-} on Co-N_x site, *Chemosphere*, 2022, **295**, 133946.
- 59 L. Xu and J. Wang, Magnetic Nanoscaled Fe₃O₄/CeO₂ Composite as an Efficient Fenton-Like Heterogeneous Catalyst for Degradation of 4-Chlorophenol, *Environ. Sci. Technol.*, 2012, **46**(18), 10145–10153.
- 60 W. Du, Q. Zhang, Y. Shang, W. Wang, Q. Li and Q. Yue, *et al.*, Sulfate saturated biosorbent-derived Co-S@NC nanoarchitecture as an efficient catalyst for peroxymonosulfate activation, *Appl. Catal., B*, 2020, **262**, 118302.
- 61 J. Lee, U. von Gunten and J. H. Kim, Persulfate-Based Advanced Oxidation: Critical Assessment of Opportunities and Roadblocks, *Environ. Sci. Technol.*, 2020, **54**(6), 3064–3081.
- 62 M. Xu, J. Li, Y. Yan, X. Zhao, J. Yan and Y. Zhang, *et al.*, Catalytic degradation of sulfamethoxazole through peroxymonosulfate activated with expanded graphite loaded CoFe₂O₄ particles, *Chem. Eng. J.*, 2019, **369**, 403–413.
- 63 J. Wei, Z. Xiong, M. Ao, Z. Guo, J. Zhang and B. Lai, *et al.*, Selective degradation of sulfamethoxazole by N-doped iron-based carbon activated peroxymonosulfate: Collaboration of singlet oxygen and high-valent iron-oxo species, *Sep. Purif. Technol.*, 2022, **297**, 121379.
- 64 Y. Jiang and Y. Lu, Designing transition-metal-boride-based electrocatalysts for applications in electrochemical water splitting, *Nanoscale*, 2020, **12**(17), 9327–9351.
- 65 B. Xu, Z. Luo, T. Tao and Y. Wang, Dual acceleration of Co(III)/Co(II) redox cycle boosts peroxymonosulfate activation for superfast chloramphenicol degradation, *Sep. Purif. Technol.*, 2024, **334**, 126321.
- 66 A. U. R. Bacha, I. Nabi, H. Cheng, K. Li, S. Ajmal and T. Wang, *et al.*, Photoelectrocatalytic degradation of endocrine-disruptor bisphenol – A with significantly activated peroxymonosulfate by Co-BiVO₄ photoanode, *Chem. Eng. J.*, 2020, **389**, 124482.
- 67 A. L. Boreen, W. A. Arnold and K. McNeill, Photochemical Fate of Sulfa Drugs in the Aquatic Environment: Sulfa Drugs Containing Five-Membered Heterocyclic Groups, *Environ. Sci. Technol.*, 2004, **38**(14), 3933–3940.
- 68 L. J. Martinez, R. H. Sik and C. F. Chignell, Fluoroquinolone Antimicrobials: Singlet Oxygen, Superoxide and Phototoxicity, *Photochem. Photobiol.*, 1998, **67**(4), 399–403.
- 69 W. A. Arnold, Y. Oueis, M. O'Connor, J. E. Rinaman, M. G. Taggart and R. E. McCarthy, *et al.*, QSARs for phenols and phenolates: oxidation potential as a predictor of reaction rate constants with photochemically produced oxidants, *Environ. Sci.: Processes Impacts*, 2017, **19**(3), 324–338.